

Mesoporous MnO/C composite synthesised from the precursor of $\text{Mn}_3(\text{C}_6\text{H}_5\text{O}_7)_2$ and the application in Li-ion batteries

Bao Shanshan¹, Li Junfeng¹ ✉, Gao Yang¹, Li Ping¹, Yue Bo², Li Yanjun², Sun Wenxian², Lai Xuefei³

¹College of Materials, Chemistry and Chemical Engineering, Chengdu University of Technology, Chengdu, 610059, Sichuan, People's Republic of China

²Sichuan Keneng Lithium Battery Co., Ltd, Chengdu, 610101, People's Republic of China

³College of Chemical Engineering, Sichuan University, Chengdu 610064, Sichuan, People's Republic of China

✉ E-mail: lijunfeng@cdut.cn

Published in Micro & Nano Letters; Received on 20th June 2018; Revised on 26th August 2018; Accepted on 24th September 2018

A facile and scalable route for the in-situ synthesis of porous MnO/C nanocomposite by annealing $\text{Mn}_3(\text{C}_6\text{H}_5\text{O}_7)_2$ precursor has been developed. MnO particles were encapsulated inside the carbon matrix to form a skeletal architecture. Such a mesoporous structure provided more active sites and effective channels for Li^+ and electrolyte, and act as the supporting structure for MnO particles during the cycling process. As an anode material for lithium ion batteries, the porous MnO/C composite had a specific capacity of 831.7 mAh g^{-1} at 100 mA g^{-1} and delivered a stable cycling capacity of 564.1 mAh g^{-1} after 59 cycles, indicating that the porous MnO/C nanocomposite could significantly improve the structural stability and might be a suitable electrode material for lithium-ion batteries.

1. Introduction: Lithium ion batteries (LIBs) have widely applied in portable electronic devices and electric vehicles due to their high-energy density and excellent cycle performance. The application of commercial graphite is limited by its low-theoretical specific capacity ($\sim 372 \text{ mAh g}^{-1}$). In recent years, extensive efforts have been devoted to the development of superior electrode materials. Transition metal oxides such as ZnO [1], MnO [2], Fe_3O_4 [3], Fe_2O_3 [4], Co_3O_4 [5] and SnO_2 [6] have been widely investigated as the next generation redox-based anode materials for LIBs. MnO has been considered as one of the promising electrode materials. MnO has the high-theoretical capacity (755.6 mAh g^{-1}), low-electrochemical motivation force (1.032 versus Li/Li^+), good safety and abundant resource [2, 7]. However, the intrinsic low-electronic conductivity, drastic volume change ($\sim 200\%$) and aggregation during the repeated cycling process are considered as the main problems to be solved in the development of MnO [8].

Considerable efforts have been made to improve the structural stability and cycling performance of MnO. The conventional modification approaches include dimension reduction, doping, morphology control and surface coating [2, 9–11]. Carbon coating (graphene, carbon nanotubes, carbon nanofilms, porous carbon) has been proven to be an effective way that can improve the electrochemical performance of MnO. For example, graphene-supported MnO nanocomposite has been recently recognised as an advisable strategy to develop the advanced electrodes for LIBs [12–14]. The synthesised graphene-supported composite possessed a desirable initial capacity ($\geq 1000 \text{ mAh g}^{-1}$) and excellent cyclic stability (the capacity retention of samples reached 95%) [13]. However, the high cost of graphene limits the large-scale application of MnO/graphene anode materials. MnO/C with the multi-architecture framework can achieve a highly reversible specific capacity and cycling stability [15–17]. The MnO/C core-shell nanowires delivered a reversible capacity of 903 mAh g^{-1} at 100 mA g^{-1} after 100 cycles and exhibited good cycling stability [15]. Similarly, the MnO/C composite with three-dimensional (3D) carbon framework exhibited a highly reversible specific capacity and excellent cycling stability [16]. The MnO/C nanocomposites consisted of nanorods and nano-octahedra (denoted as nRO-MnO/C) showed a reversible capacity of 861.3 mAh g^{-1} after 120 cycles even at a rate of 0.13 C [18]. Therefore, the design of MnO decorated with

carbon is an effective way to reduce the volume effect and improve the stability of pure MnO.

In this study, the porous MnO/C nanocomposite was successfully synthesised through a scalable co-precipitation approach. This method did not require an additional carbon source. In a typical synthesis process, the hydroxy groups of citrate locked and fixed Mn^{2+} and MnO was in-situ formed after the precursor was carbonised in an argon atmosphere. Finally, the MnO/C composite with MnO nanoparticles dispersed in the porous carbon layer was obtained. Since the finest MnO particles encapsulated inside the porous carbon matrix could effectively buffer the volume change of MnO, the porous MnO/C composite applied as the electrode material of LIBs showed the excellent cycling stability.

2. Experiment section

2.1. Preparation of materials: The porous MnO/C composite was prepared by the co-precipitation method. In this study, manganese chloride ($\text{MnCl}_2 \cdot 4\text{H}_2\text{O}$, $\geq 99\%$, KeLong Chemical Co., Ltd, Chengdu, China), trisodium citrate dihydrate ($\text{Na}_3\text{C}_6\text{H}_5\text{O}_7 \cdot 2\text{H}_2\text{O}$, $\geq 99\%$, KeLong Chemical Co., Ltd, Chengdu, China) and ethanol ($\text{C}_2\text{H}_6\text{O}$, AR, $\geq 99.7\%$) were used as starting materials. In a typical synthesis of precursors, the molar ratio for Mn^{2+} and $\text{C}_6\text{H}_5\text{O}_7^{3-}$ was 3:2. Firstly, 0.15 mmol of $\text{MnCl}_2 \cdot 4\text{H}_2\text{O}$ and 0.1 mmol of $\text{Na}_3\text{C}_6\text{H}_5\text{O}_7$ were dissolved in 20 ml of deionised water to form a homogeneous solution under continuous stirring. Then 20 ml of absolute ethyl alcohol was added into the mixed solution. The precipitates were centrifuged and washed three times with the mixed solution of ethanol and deionised water, followed by freeze-drying under vacuum overnight. In the following process, the as-prepared precursor was further annealed at 800°C for 3 h under argon flow. Finally, the porous MnO/C composite was obtained after the decomposition of $\text{Mn}_3(\text{C}_6\text{H}_5\text{O}_7)_2$ precursor.

2.2. Material characterisation: The phase structure and crystallinity of the as-prepared MnO/C composites were characterised by the powder X-ray diffraction (XRD, DX-2700) with $\text{Cu K}\alpha$ ($\lambda = 0.15406 \text{ nm}$). The average crystallite size can be calculated by using the Scherrer equation. The transmission electron microscopy (TEM) images were examined by JEOL-JEM-100CX microscopy, under an acceleration voltage of 80 kV .

The thermostability was obtained on a thermo-gravimetric analyser (STA-409-PC/PG) at a heating rate of $15^{\circ}\text{C min}^{-1}$ in an argon atmosphere. Raman spectra (Raman, Invia) were obtained with an Ar^{+} laser (532 nm). The X-ray photoelectron spectroscopy (XPS, ESCALAB 250Xi) was used to analyse the chemical composition and the valence states of constituent elements. The porous character of the products was performed by an N_2 adsorption measurement instrument (Quantachrome Instrument, America) with a NOVA 2000e evaluation system.

2.3. Electrochemical characterisation: A standard CR2032-type coin cell was assembled to investigate the electrochemical characters. The coating electrode materials were prepared by mixing 70 wt% porous MnO/C composites, 20 wt% Polyvinylidene fluoride (S130), and 10 wt% acetylene black, then stirred constantly in a closed vessel, followed by coating on copper foil. The thickness of the electrode film was 150 μm . Coin cell batteries were assembled in an argon-filled glovebox (Mikrouna (China) Co. Ltd 1220/750). The electrolyte was 1 M LiPF_6 solution in ethylene carbonate and dimethyl carbonate solution (1:1). The charge/discharge cycling performance and the rate performance were determined on a NEWARE automatic battery tester (NEWARE BTS-4000, CT-4008, Wuhan, China) under the voltage window of 0.01–3.0 V (versus Li/Li^{+}). Cyclic voltammetry was taken on an electrochemical workstation (CS350, Wuhan) at a scanning rate of 0.1 mV/s.

3. Results and discussion

3.1. Characterisation of $\text{Mn}_3(\text{C}_6\text{H}_5\text{O}_7)_2$ precursor: Fig. 1 shows the crystalline structure and morphology of $\text{Mn}_3(\text{C}_6\text{H}_5\text{O}_7)_2$ precursor prepared with the co-precipitation method. As shown in XRD patterns in Fig. 1a, no apparent diffraction peak is observed except a drum-like broad peak, indicating that the precursor is a typical citrate complex with the amorphous structure and low crystallinity, which is ascribed to the unstable chelated structure formed by $\text{C}_6\text{H}_5\text{O}_7^{3-}$ and Mn^{2+} [19]. The morphological character is shown in Fig. 1b. The precursors with the non-uniform particle size were observed and the size ranged from 2 to 10 μm shows the crystalline structure and morphology of $\text{Mn}_3(\text{C}_6\text{H}_5\text{O}_7)_2$ precursors prepared with the co-precipitation method. As shown in XRD patterns in Fig. 1a, there is no any apparent diffraction peak except a drum-like broad peak. It indicates that the as-obtained precursor is in an amorphous state, which may be ascribed to the chelated structure formed by $\text{C}_6\text{H}_5\text{O}_7^{3-}$ and Mn^{2+} is unstable [20]. The morphological character is shown in Fig. 1b. A small number of irregular particles can be observed. The scanning electron microscopy (SEM) image also clearly shows that the precursors are aggregated to form a number of grains with the non-uniform particle size distribution in the range of 2 to 10 μm .

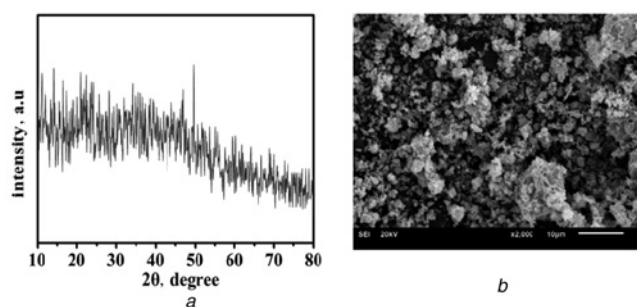


Fig. 1 Crystalline structure and morphology of the as-prepared precursor
a XRD pattern
b SEM image

To further gain the thermodynamics behavior of $\text{Mn}_3(\text{C}_6\text{H}_5\text{O}_7)_2$, the TGA analysis in argon atmosphere was performed. It could be used to analyse the decomposition of $\text{Mn}_3(\text{C}_6\text{H}_5\text{O}_7)_2$ and provide important data for the following carbonisation process. The TG curve (Fig. 2) shows a significant weight loss (63.6%) from 30 to 1000 $^{\circ}\text{C}$. The weight loss can be ascribed to the dehydration of $\text{Mn}_3(\text{C}_6\text{H}_5\text{O}_7)_2$ and the formation of MnO. Some gases such as CO and CH_4 can effectively facilitate the pore-forming [20]. Based on the TG results, we chose 800 $^{\circ}\text{C}$ as the carbonisation temperature.

3.2. Structure feature of the porous MnO/C composite: Fig. 3 shows the XRD pattern of the MnO/C composite annealed at 800 $^{\circ}\text{C}$ for 3 h in an argon atmosphere. The diffraction peaks at 35° , 41° , 59° , 70° and 74° were well consistent with standard face-centred cubic MnO (JCPDS Card No. 07-0230 MnO, $a=b=c=4.445 \text{ \AA}$. Space group: $Fm-3m$), whereas the small peaks corresponding to tetragonal Mn_3O_4 (JCPDS Card No. 01-1127, $a=b=5.75 \text{ \AA}$, $c=9.42 \text{ \AA}$) were attributed to the oxidation–reduction reaction between MnO and pyrolytic carbon in an argon atmosphere.

Fig. 4 shows the Raman spectra of the porous MnO/C composite. Two apparent peaks at 1344 and 1596 cm^{-1} were ascribed to the defect-based D band (D band) and the crystalline G band (G band) of carbon, respectively. A large number of structure defects were found when the ratio of I_D/I_G was close to 1 [21, 22]. The intensity ratio of I_D/I_G was 0.84, revealing the existence of amorphous carbon in the MnO/C composite. The amorphous carbon layer could effectively buffer the volume change and facilitate the cross-linking between MnO and electrolyte. An obvious vibrational band at $\sim 646 \text{ cm}^{-1}$ was ascribed to the symmetric stretching of the

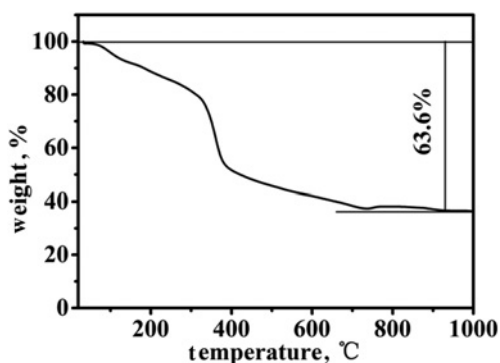


Fig. 2 TG curve of manganese citrate under argon atmosphere from 30 to 1000 $^{\circ}\text{C}$

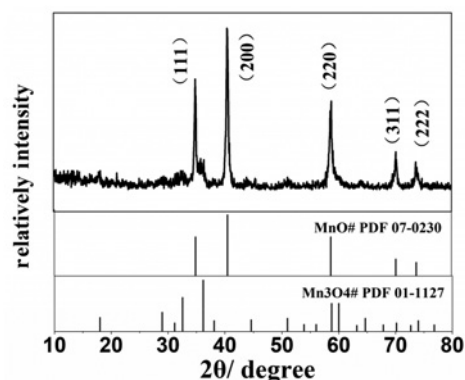


Fig. 3 XRD pattern of MnO/C composite

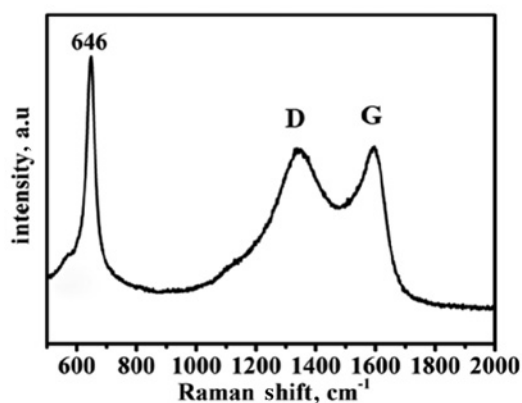


Fig. 4 Raman spectra of the MnO/C composite

Mn₃O₄ group [15, 16, 23]. The result was consistent with XRD results.

To confirm the chemical bonding state of the porous MnO/C composite, XPS analysis was conducted (Fig. 5). The main peaks in Fig. 5a were C 1s (284.75 eV), O 1s (530.18 eV), and Mn 2p (642.48 and 653.98 eV). Fig. 5b verifies the presence of both Mn²⁺ and Mn³⁺ in the composite. The values of Mn 2p_{3/2} and Mn 2p_{1/2} (Fig. 5b) were, respectively, 642.3 and 653.9 eV, which were consistent with previous reports on MnO [16, 24]. The separation of 11.8 eV between peaks at 643.8 and 655.6 eV is characteristic of Mn₃O₄, in which probably due to the partial oxidation of MnO [25]. In Fig. 5c, two peaks at 531.8 and 530.2 eV were ascribed to MnO [26]. The peak at 533.4 eV was related to surface OH and COOH groups (Fig. 5c). The C1 spectrum is shown in Fig. 5d. The main peak at 284.7 eV belongs to the C–C bond in the carbon network. Two peaks at 285.8 and 288.3 eV were ascribed to the graphitic carbon (C–O) and O–C=O bond, respectively. The XPS spectra are consistent with the XRD results and Raman spectra. In addition, according to the calculation based on the XPS spectrum, the percentages of Mn, C and O were 11.78, 53.44 and 34.78 At.%, respectively.

Fig. 6 shows the morphology and microstructure feature of the porous MnO/C composite. There is no particular morphological

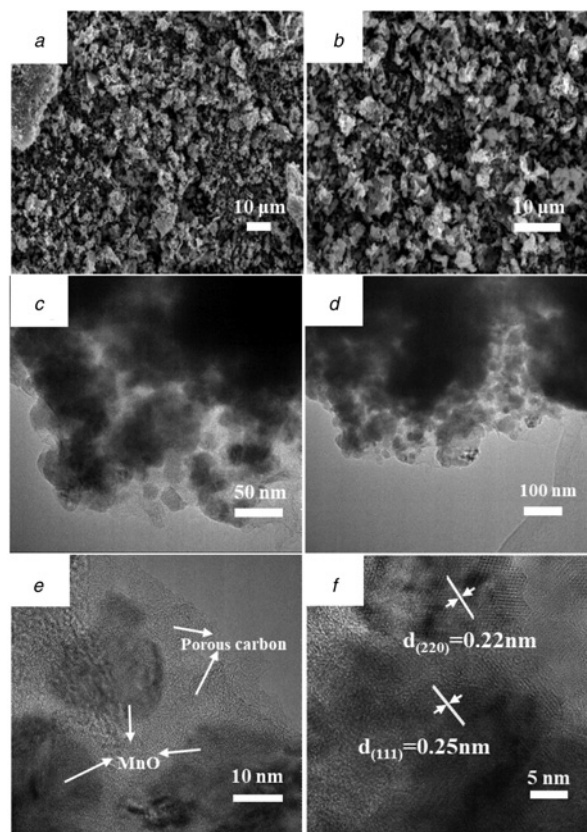


Fig. 6 SEM and TEM images of MnO/C composites

a, b SEM images
c, d, e, f TEM images

character in a size range from 3–10 μm (Figs. 6a and b). A detailed microstructure feature was further explored by TEM. In Figs. 6c and d, MnO particles are encapsulated inside the carbon matrix. Meanwhile, Fig. 6e demonstrates the porous character of carbon and a skeletal architecture with interconnecting nanoparticles [16]. The interplanar spacings for encapsulated nanoparticles are, respectively, 0.25 and 0.22 nm (Fig. 6f), which correspond to (111) and (220) planes of MnO [18].

It is well known that the pore structure plays an important role in a composite. The micro-pore character was investigated with nitrogen adsorption/desorption in Brunauer–Emmett–Teller (BET) analysis. The nitrogen adsorption/desorption isotherms and corresponding pore size distribution (inset) are clearly shown in Fig. 7. The isotherm curve presents an apparent IV-shape with a Type H2 hysteresis at a relative pressure of 0.4–1, indicating the existence of the mesoporous structure. These results are consistent with TEM images. The pore size distribution curve (inset in Fig. 7) was determined with the adsorption branches of the isotherms according to the Barrett–Joyner–Halenda method. According to the BET calculation, the specific surface area is 10.482 m² g^{−1} and the pore size distribution is mainly centred at 18.873 nm. Consequently, the mesoporous structure and narrow pore size distribution improve the electrochemical properties of MnO by providing more active sites and effective channels for Li⁺ and electrolyte.

3.3 Electrochemical properties: Based on the structural features of the MnO/C composite, we further evaluated their electrochemical performances as an anode material for LIBs. Fig. 8a shows the 1st, 2nd, 10th, 20th and 50th charge/discharge profile of the composite at the current of 100 mA g^{−1}. Clearly, an obvious plateau observed in the initial discharge process related to the

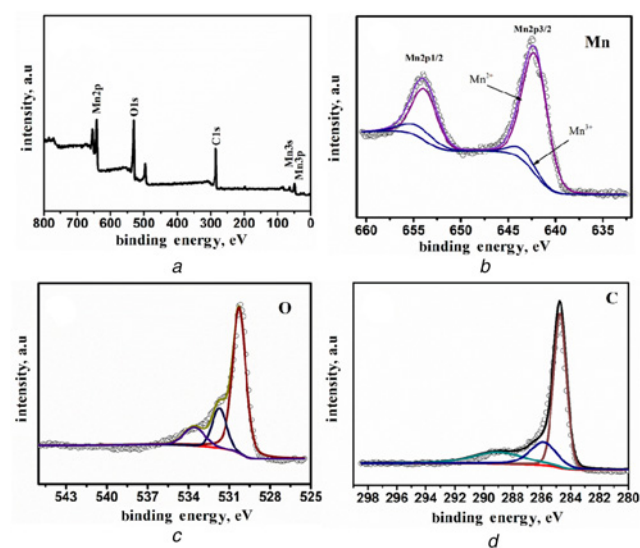


Fig. 5 XPS spectra of the porous MnO/C composite

a Survey spectrum
b Mn
c O
d C

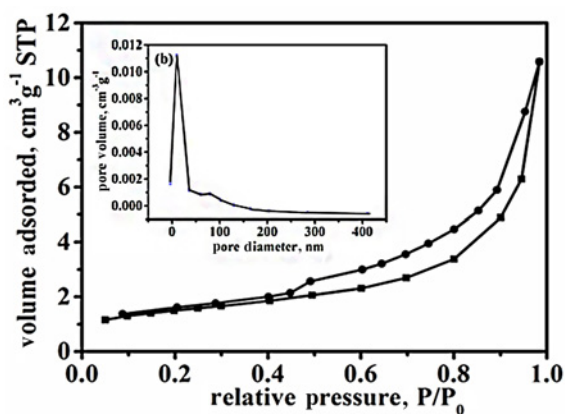


Fig. 7 Nitrogen adsorption–desorption isotherms and the pore size distributions (inset)

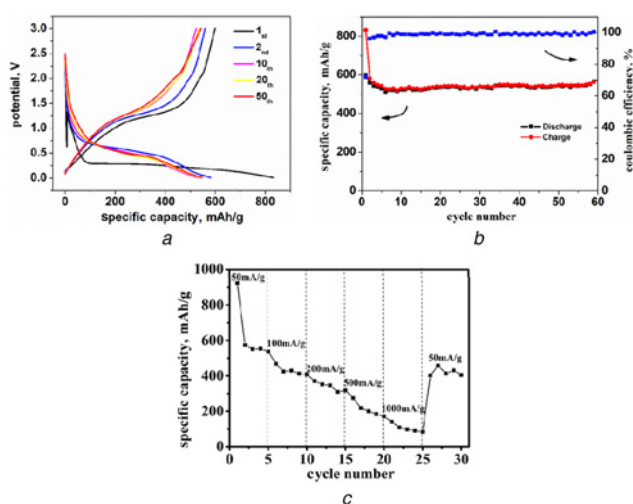


Fig. 8 Electrochemical properties of MnO/porous carbon composite
 a Galvanostatic discharge/charge profiles of the composite at a current rate of 100 mA/g
 b Cycling performance at a current rate of 100 mA/g
 c Rate capability test at the current densities of 50, 100, 200, 500 and 1000 mA/g, respectively

reduction of MnO into Mn and the formation of Li_2O ($\text{MnO} + 2\text{Li}^+ + 2\text{e}^- \rightarrow \text{Mn} + \text{Li}_2\text{O}$) appears at 0.25 V and then shift to 0.5 V in the following cycles. The variation of potential may be associated with the pulverisation of active materials and the formation of solid electrolyte interphase [27, 28]. For the charge process, the plateau at around 1.3 V was ascribed to the oxidation of Mn to MnO ($\text{Mn} - 2\text{e}^- + \text{Li}_2\text{O} \rightarrow \text{MnO} + 2\text{Li}^+$) [18, 29]. The discharge/charge curve was almost overlapped from 10th to 50th cycles due to the improved reaction kinetics after the first cycle and the synergistic effect between porous carbon and MnO nanoparticles [30].

The cycling performance and corresponding coulombic efficiency of the porous MnO/C composite at 100 mA g^{-1} are shown in Fig. 8b. The initial discharge/charge capacities of the MnO/C composite are, respectively, 831.7 and 599.1 mAh g^{-1} , and corresponding coulombic efficiency is 72.1%. The irreversible capacity loss in the first cycle is mainly caused by the irreversible reaction between active materials and electrolyte [27, 28]. After 59 cycles, the reversible discharge and charge capacities are, respectively, 564.1 and 566.5 mAh g^{-1} , with the coulombic efficiency of 100.4%. From the 10th to 59th cycles, about 97% of the discharge capacity is maintained due to the activation of MnO encapsulated

inside the carbon layer, and the reversible growth of a polymeric gel-like film caused by the degradation of activated electrolyte [31, 32]. It demonstrates that MnO coated with porous carbon can improve the structural stability.

Fig. 8c displays the rate capability of the porous MnO/C composite at the current density from 0.05 to 1 mA g^{-1} . The discharge capacity was maintained at 550 mAh g^{-1} in the first 5 cycles. When the current density rose to 1000 mA g^{-1} , the rate capability of the porous MnO/C composite decreased quickly, retaining only 429, 340, 210 and 104 mAh g^{-1} , respectively. When the current density returned to 50 mA g^{-1} , the capacity of 420 mAh g^{-1} was restored again. The poor rate capability was ascribed to MnO which was decorated with an amorphous carbon layer and unable to offer the excellent conductivity for rapid electron transfer under high-current density [33].

4. Conclusion: In this study, the porous MnO/C composite was in-situ synthesised through a facile and scalable route under mild reaction conditions in good yields. As an anode material for LIBs, the porous MnO/C composite had a specific capacity of 831.7 mAh g^{-1} at 100 mA g^{-1} and delivered a cycling capacity of 564.1 mAh g^{-1} after 59 cycles. The good cyclic performance was ascribed to the MnO particles encapsulated in the amorphous carbon matrix, which could provide a support for MnO particles during the cycling process and facilitate the transport of Li^+ and electrolyte. The study provides the basis for the application of mesoporous MnO/C composites as anode materials in the next-generation LIBs.

5. Acknowledgments: This work was supported by the Major Project of Sichuan Provincial Department of Education (grant no. 18ZA0062), the Science and Technology Department Project of Sichuan Province (grant nos. 2015GZ0054 and 2016GZ0283), and the Research Project of Experimental Area for Strategic Resource Innovation and Development of Panxi (grant no. CDWA2016ZC3-1).

6 References

- [1] Zhang G., Zhang H., Zhang X., *ET AL.*: ‘Solid-solution-like ZnO/C composites as excellent anode materials for lithium ion batteries’, *Electrochim. Acta*, 2015, **186**, pp. 165–173
- [2] Zhong K., Xia X., Zhang B., *ET AL.*: ‘MnO powder as anode active materials for lithium ion batteries’, *J. Power Sources*, 2010, **195**, (10), pp. 3300–3308
- [3] Ren M., Yang M., Liu W., *ET AL.*: ‘Ultra-small Fe_3O_4 nanocrystals decorated on 2D graphene nanosheets with excellent cycling stability as anode materials for lithium ion batteries’, *Electrochim. Acta*, 2016, **194**, pp. 219–227
- [4] Hwang S.W., Umar A., Kim S.H.: ‘Iron oxide ($\alpha\text{-Fe}_2\text{O}_3$) nanoparticles as an anode material for lithium ion battery’, *J. Nanosci. Nanotechnol.*, 2015, **15**, (7), pp. 5129–5134
- [5] Wu Z.S., Ren W., Wen L., *ET AL.*: ‘Graphene anchored with Co_3O_4 nanoparticles as anode of lithium ion batteries with enhanced reversible capacity and cyclic performance’, *ACS Nano*, 2010, **4**, (6), pp. 3187–3194
- [6] Wang Y., Guo W., Yang Y., *ET AL.*: ‘Rational design of $\text{SnO}_2@\text{C}@\text{MnO}_2$ hierarchical hollow hybrid nanospheres for a Li-ion battery anode with enhanced performances’, *Electrochim. Acta*, 2018, **262**, pp. 1–8
- [7] Wang H., Cui L.F., Yang Y., *ET AL.*: ‘Cheminform abstract: Mn_3O_4 -graphene hybrid as a high-capacity anode material for lithium ion batteries’, *Cheminform*, 2011, **42**, pp. 13978–13980
- [8] Mai Y.J., Zhang D., Qiao Y.Q., *ET AL.*: ‘MnO/reduced graphene oxide sheet hybrid as an anode for Li-ion batteries with enhanced lithium storage performance’, *J. Power Sources*, 2012, **216**, (11), pp. 201–207
- [9] Yu X.Q., He Y., Sun J.P., *ET AL.*: ‘Nanocrystalline MnO thin film anode for lithium ion batteries with low overpotential’, *Electrochem. Commun.*, 2009, **11**, (4), pp. 791–794
- [10] Shen L., Liu Y.: ‘Brain-like manganese monoxide microspheres as anode materials for lithium ion battery’, *Chem. Phys. Lett.*, 2017, **677**, pp. 167–171

- [11] Zhang L., Song J., Liu Y., *ET AL.*: 'Tailoring nanostructured MnO₂ as anodes for lithium ion batteries with high reversible capacity and initial coulombic efficiency', *J. Power Sources*, 2018, **379**, pp. 68–73
- [12] Lu S., Gao Y., Li Z., *ET AL.*: 'Hierarchical hybrid sandwiched structure of ultrathin graphene nanosheets enwrapped MnO nanooctahedra with excellent lithium storage capability', *J. Alloys Compd.*, 2018, **749**, pp. 424–432
- [13] Wang J., Deng Q., Li M., *ET AL.*: 'High-capacity and long-life lithium storage boosted by pseudocapacitance in three-dimensional MnO-Cu-CNT/graphene anodes', *Nanoscale*, 2018, **10**, (6), pp. 2944–2954
- [14] Wang F., Cai J., Yu J., *ET AL.*: 'Simultaneous electrospinning and electrospraying: fabrication of a carbon nanofibre/MnO/reduced graphene oxide thin film as a high-performance anode for lithium-ion batteries', *Chemelectrochem*, 2018, **5**, (1), pp. 51–61
- [15] Zhang C., Wang J.-G., Jin D., *ET AL.*: 'Facile fabrication of MnO/C core-shell nanowires as an advanced anode material for lithium-ion batteries', *Electrochim. Acta*, 2015, **180**, pp. 990–997
- [16] Jia J., Hu X., Wen Z.: 'Robust 3D network architectures of MnO nanoparticles bridged by ultrathin graphitic carbon for high-performance lithium-ion battery anodes', *Nano Res.*, 2017, **11**, (2), pp. 1135–1145
- [17] Qu E., Chen T., Xiao Q., *ET AL.*: 'Coaxial MnO₂ nanoshell/CNFs composite film anode for high-performance lithium-ion batteries', *J. Electrochem. Soc.*, 2018, **165**, (3), pp. A487–A492
- [18] Xu Y.-F., Xu G.-L., Su H., *ET AL.*: 'Porous MnO/C of composite nanostructure consisting of nanorods and nano-octahedra as anode of lithium ion batteries with enhanced electrochemical performances', *J. Alloys Compd.*, 2016, **676**, pp. 156–163
- [19] Kim S.G., Wang W.N., Iwaki T., *ET AL.*: 'Low-temperature crystallization of barium ferrite nanoparticles by a sodium citrate-aided synthetic process', *J. Phys. Chem. C*, 2007, **111**, (28), pp. 1–121
- [20] Zhou Q.Q., Chen X.Y., Wang B.: 'An activation-free protocol for preparing porous carbon from calcium citrate and the capacitive performance', *Microporous Mesoporous Mater.*, 2012, **158**, pp. 155–161
- [21] Fu L., Tang K., Song K., *ET AL.*: 'Nitrogen doped porous carbon fibres as anode materials for sodium ion batteries with excellent rate performance', *Nanoscale*, 2014, **6**, (3), pp. 1384–1389
- [22] Li Z., Mi Y., Liu X., *ET AL.*: 'Flexible graphene/MnO₂ composite papers for supercapacitor electrodes', *J. Mater. Chem.*, 2011, **21**, (38), pp. 14706–14711
- [23] Zhu W., Huang H., Zhang W., *ET AL.*: 'Synthesis of MnO/C composites derived from pollen template for advanced lithium-ion batteries', *Electrochim. Acta*, 2015, **152**, pp. 286–293
- [24] Liu C., Zhang C., Song H., *ET AL.*: 'MnO nanoparticles with cationic vacancies and discrepant crystallinity dispersed into porous carbon for Li-ion capacitors', *J. Mater. Chem. A*, 2016, **4**, (9), pp. 3362–3370
- [25] Li T., Xue B., Wang B., *ET AL.*: 'Tubular monolayer superlattices of hollow Mn₃O₄ nanocrystals and their oxygen reduction activity', *J. Am. Chem. Soc.*, 2017, **139**, (35), pp. 12133–12136
- [26] Zhang Q., Wang W., Jiang D., *ET AL.*: 'Mesoporous activated carbon decorated with MnO as anode materials for lithium ion batteries', *J. Mater. Sci.*, 2016, **51**, (7), pp. 3536–3544
- [27] Wang J., Du N., Wu H., *ET AL.*: 'Order-aligned Mn₃O₄ nanostructures as super high-rate electrodes for rechargeable lithium-ion batteries', *J. Power Sources*, 2013, **222**, (2), pp. 32–37
- [28] Fan X., Li S., Lu L.: 'Porous micrometer-sized MnO cubes as anode of lithium ion battery', *Electrochim. Acta*, 2016, **200**, pp. 152–160
- [29] Sun B., Chen Z., Kim H.S., *ET AL.*: 'MnO/C core-shell nanorods as high capacity anode materials for lithium-ion batteries', *J. Power Sources*, 2011, **196**, (6), pp. 3346–3349
- [30] Ding C., Huang X., Zhang H., *ET AL.*: 'Self-assembled porous Fe₃O₄/C nanoclusters with superior rate capability for advanced lithium-ion batteries', *J. Mater. Sci. Mater. Electron.*, 2018, **29**, (8), pp. 6491–6500
- [31] Wang R., Cao L., Li J., *ET AL.*: 'Design of dual-carbon modified MnO electrode improves adsorption and conversion reaction in Li-ion batteries', *Ceram. Int.*, 2018, **44**, (3), pp. 3248–3254
- [32] Zhu J., Wang T., Fan F., *ET AL.*: 'Atomic-scale control of silicon expansion space as ultrastable battery anodes', *ACS Nano*, 2016, **10**, (9), pp. 8243–8251
- [33] Zhang S., He W., Zhang X., *ET AL.*: 'Rational design of carbon-coated hollow MnO nanotubes for Li-ion batteries', *J. Mater. Sci. Mater. Electron.*, 2015, **26**, (4), pp. 2189–2197